

**A GENERALIZED FINITE SIZED DIPOLE MODEL FOR
RADAR AND MEDICAL IMAGING PART II: NEAR FIELD
FORMULATION FOR MAGNETIC RESONANCE IMAGING**

T. S. Naveendra

RF and Radios Division
CET Technologies Pte Ltd.,
Singapore Technologies Electronics,
Singapore Technologies Building,
Singapore 609602

P. R. P. Hoole

Division of Communications Engineering,
School of Electrical and Electronic Engineering
Nanyang Avenue, Block S1,
Nanyang Technological University
Singapore 639798

1. Introduction

2. Basics of MRI

- 2.1 Nuclear Precession
- 2.2 Longitudinal Relaxation
- 2.3 Nuclear Magnetic Resonance
- 2.4 Rotating Frame
- 2.5 Transverse Relaxation
- 2.6 Imaging Techniques
 - 2.6.1 Back Projection Imaging
 - 2.6.2 Fourier Imaging

3. Near Electromagnetic Fields in MRI Technology

- 3.1 Bloch Equations
- 3.2 Electromagnetic Fields due to the Resonating Nuclear Magnetic Moment

- 3.2.1 Magnetic Fields due to the Magnetic Moment along the x axis
- 3.2.2 Magnetic Fields due to the Magnetic Moment along the y axis
- 3.2.3 Resultant Magnetic Fields at $P(r, \theta)$
- 3.3. Magnetic Resonance Time Domain Signal
 - 3.3.1 Ensemble of Signals from Radiating Regions
- 4. **Magnetic Resonance Image Results**
 - 4.1 H_r Based Image
 - 4.2 H_θ Based Image
 - 4.3 Image due to Circularly Polarized Signals
- 5. **Correction for Intensity Inhomogeneity Artifact**
 - 5.1 Correction for Phase Modifying Factor
 - 5.2 Correction Algorithm for Magnitude Modifying Factor
 - 5.2.1 MMF Block
 - 5.2.2 Post Processing Block
 - 5.3 Corrected Image
- 6. **Conclusions**
- References**

1. INTRODUCTION

Magnetic Resonance Imaging (MRI) is a non-invasive biomedical imaging technique. It is used to obtain high-resolution images of the human body at any required cross section. Newer techniques have been adapted to perform volume and flow imaging too. Hence it could be considered a comprehensive imaging method. It is considered to be the safest and most efficient of contemporary imaging methods. The underlying principle is based on nuclear magnetic resonance. The signals used in the excitation and the signals obtained from this process are electromagnetic in nature [1, 2]. By appropriate signal processing, images are formed from these signals. Hence there is impetus to look at the present signal model and see whether this could be refined in any manner to yield better understanding of the intensity inhomogeneity artifact found in the images formed. The basic mechanism of magnetic resonance and the electromagnetic fields created by the nuclei have been looked into from a new perspective and the image results are presented. Emphasis is on analyzing the effects of the near electromagnetic fields on the synthesized MRI images.

In section 2, the basics of the nuclear resonance phenomenon and magnetic resonance imaging techniques are presented. In section 3 the equation of motion of resonating atomic nuclei is presented mathematically and the magnetic moment in the imaging plane under consideration is reformulated as a combination of two orthogonal magnetic moments that are 90° out of phase. It is then possible to analyze the near-field electromagnetic fields due to these magnetic moments more closely using the established field equations. Following the derivation of temporal return signals in MRI, section 4 looks at the effect of the near electromagnetic fields on the magnetic resonance images. The effect of the two factors introduced in part I, namely *Magnitude Modifying Factor (MMF)* and *Phase Modifying Factor (PMF)*, on the magnetic resonance images is studied. In section 5 is presented a correction algorithm that removes the intensity inhomogeneity artifact and image blurring due to the *MMF* and *PMF* respectively. Some useful conclusions are drawn in section 6.

2. BASICS OF MRI

2.1 Nuclear Precession

The human body is predominantly composed of hydrogen atoms. This is because the main constituent of the human body is water. The hydrogen nucleus has a positive charge located at some distance away from the center but still within the volume of the nucleus. Further, the hydrogen nucleus is spinning about an axis with an unknown rate of rotation and it does not slowdown due to friction or for any other reason. Thus as the nucleus spins, the positive charge revolves in an approximately circular path much as an electron in a loop or wire. This movement of the positive charge produces a magnetic field and thus a magnet of microscopic scale is created. When this nucleus is subjected to a constant magnetic field B it tends to align with this field. However as the nucleus itself is spinning it wobbles too. This wobbling motion is called precession. This precession has a fixed frequency, being proportional to the strength of the applied magnetic field and the fixed frequency is called the Larmor frequency of the nucleus. The Larmor frequency will be the natural frequency of the nucleus at the particular applied magnetic field strength. This motion is similar to the motion of a spinning top which wobbles due to the earth's gravitational field. The relationship between the applied magnetic field and

the frequency of precession, a relationship which is central to MRI, is given by [1]

$$\omega_o = -\gamma H_o \quad (2.1)$$

The precessionary motion of the macroscopic magnetic dipole M is shown in Fig. 2.1.

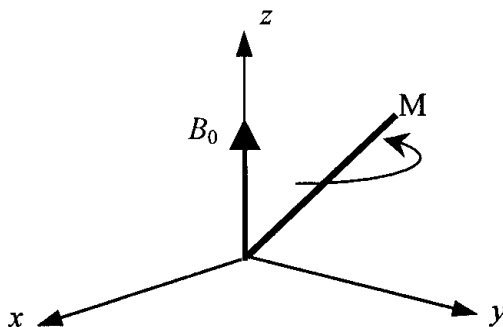


Figure 2.1 Precessionary motion.

In addition to the external magnetic field B_o a nucleus will experience small additional fields generated by neighbouring current loops, which may be intramolecular or intermolecular in nature. Because the molecules tumble and exhibit rapid and random motion, the total magnetic field experienced by each molecule fluctuates. These fluctuations can be considered to be parallel or perpendicular to B_o .

2.2 Longitudinal Relaxation

In trying to bring the nuclear magnet into alignment with the applied magnetic field B_o the energy of the molecule is reduced (the energy steady state) whereas increase in non-alignment increases its energy. As reaction and action are equal and opposite, there is with the flipping of each nuclear spin an exchange of energy with the adjacent molecules. Thus when alignment takes place a minute quantity of energy is passed to the adjacent molecules and their motion minutely increases. This is called spin-lattice interaction. The kinetic energy is removed by this mechanism and bulk magnetization is built as shown in Fig. 2.2. The time constant associated with this mechanism is called Longitudinal Relaxation time (T_1). It has been found that the bulk

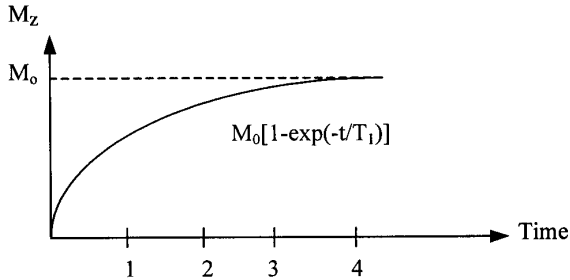


Figure 2.2 Nuclear magnetization.

magnetization built up is proportional to the applied magnetic field B_o [1].

2.3 Nuclear Magnetic Resonance

The nucleus precesses at the Larmor frequency. Hence it is possible to elicit a response using resonance principles by applying a stimulus having approximately the Larmor frequency. The stimulus employed in MRI is an additional magnetic field B_1 that rotates about B_0 close to the Larmor frequency. This causes the magnetization to precess about B_1 and induce a signal in a suitably placed coil. This is called Nuclear Magnetic Resonance (NMR) [1].

2.4 Rotating Frame

The conventional Cartesian framework (x, y, z) is shown in Fig. 2.1. The magnetic field B_o was placed in the z direction. Thus precession takes place in the xy plane and equilibrium magnetization M settles along the z -axis. For mathematical manipulation, another frame (x', y', z') which rotates about the z axis in the same direction as the precession is considered and observations are made with reference to this plane. This is called the rotating frame of reference.

When rotation equals the Larmor frequency the precession seems to have stopped with reference to the new frame. Hence in the rotating frame of reference there is no effect of the magnetic field B_0 . An additional magnetic field B_1 which rotates about B_0 at the Larmor frequency will be stationary in the rotating frame [3]. If the B_1 field is placed along the $-y'$ axis as shown in Fig. 2.3, M precesses about B_1 . Depending on the duration the excitation was applied M will settle on

the $x'y'$ plane along the x' axis as shown in Fig. 2.3. This sequence is called 90° excitation. There are other excitation sequences as well, used to impress parameters such as relaxation time, magnetization density or a combination of these on the return resonant signals.

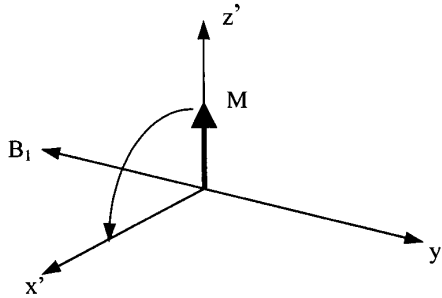


Figure 2.3 A 90° excitation magnetization.

The above explanation is true when there is resonance between B_1 and the rotating frame. Under off-resonance condition there will be relative precession between the rotating frame and B_1 . This precession could be modeled as due to an additional magnetic field ΔB_o in the z' direction. Thus the magnetization will precess under the influence of an effective field $B_{1\text{eff}}$ that is the vector sum of B_1 and ΔB_o as shown in Fig. 2.4 [1].

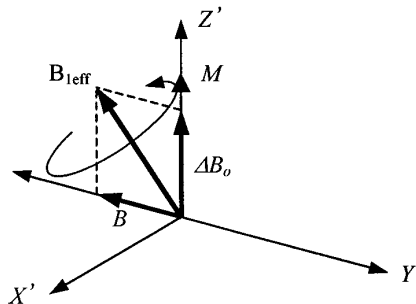


Figure 2.4 Precession under effective magnetic field.

If the stimulus is badly in error with the Larmor frequency, the resultant will be largely elevated or depressed from the $x'y'$ plane and cannot be detected. Thus significant signal is only obtained when the frequency of the stimulus is the same or nearly the same as the natural frequency of the magnetic resonance system.

2.5 Transverse Relaxation

The magnetic resonance signal induced in a coil will be as shown in Fig. 2.5. The signal decays as shown by a process termed transverse relaxation to indicate the decaying of magnetization which is transverse to the applied magnetic field. The transverse relaxation time constant T_2 is usually less than longitudinal relaxation time constant T_1 [1]. This mechanism is due to the interaction between close nuclei.

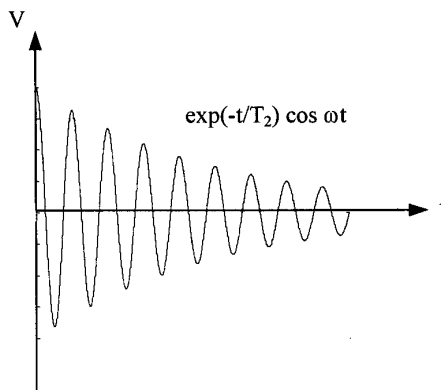


Figure 2.5 Magnetic resonance signal.

2.6 Imaging Techniques

2.6.1 Back Projection Imaging

From (2.1) it is seen that the resonant frequency in any region is dependent on the applied magnetic field strength. If a gradient magnetic field is applied, the region to be image will be frequency coded in the following form [3]

$$\omega(x) = \gamma(B_o + xG) = \omega_o + \gamma xG \quad (2.2)$$

An extension of this concept is used in back projection imaging. A one-dimensional field gradient is applied at several angles, and the nuclear magnetic resonance (NMR) spectrum is recorded for each direction. The direction of the gradient G is changed by using a combination of gradient fields G_x and G_y as

$$\begin{aligned} G_y &= G \sin \theta \\ G_x &= G \cos \theta \quad 0 \leq \theta < \pi \end{aligned} \quad (2.3)$$

Gradient G_z is used to select the slice of interest in the z direction.

The collected data can be back projected to form the image. This was the first MRI method to be demonstrated [1]. But the back projection method is not commonly used because the non-linearity of the gradient field causes image blurring [3]. This principle has been extended to form another imaging method called Fourier Imaging.

2.6.2 Fourier Imaging

In Fourier imaging a phase encoding gradient G_ϕ is introduced in addition to the slice selection and frequency encoding gradients. The phase encoding gradient is applied in a direction perpendicular to both the frequency encoding and slice selection gradients and it is used to impart a specific phase angle dependent on the location, to a transverse magnetization vector [3, 4].

When the slice selection gradient is turned on, all the radiating regions in a slice will have the same radio frequency. But when the phase encoding gradient is turned on, the resonant frequency will change in the direction of the phase encoding gradient. When it is turned off all regions will have the same frequency but different phase. Then the signals are obtained when the frequency encoding gradient is applied. Thus the regions are effectively encoded in phase and frequency in orthogonal directions. This sequence of pulses is repeated 128 or 256 times with different phase encoding gradient values, to collect all the data needed to produce an image depending on whether the image is to be created to a resolution of $1/128$ or $1/256$ of sample dimension [4].

The collected raw data is a complex signal matrix $S_{ki} = S(t_i, g_k)$, where g_k and t_i are chosen to be equi-spaced in the intervals $[-G_\phi, G_\phi]$ and $[-T, T]$ respectively [3]. where

$$g_k = \left(\frac{2G_\phi}{n} \right) k; \quad k = -\frac{1}{2}n, -\frac{1}{2}n + 1, \dots, \frac{1}{2}n - 1 \quad (2.4)$$

$$t_i = \left(\frac{2T}{m}\right) i; \quad i = -\frac{1}{2}m, -\frac{1}{2}m + 1, \dots, \frac{1}{2}m - 1 \quad (2.5)$$

A two dimensional Discrete Fourier Transform (2DFT) of the raw data will yield the final image matrix I_{sr} [3, 4].

$$I_{sr} = \left| \sum_{i=-m/2}^{m/2-1} \sum_{k=-n/2}^{n/2-1} s_{kj} \exp 2\pi j \left(\frac{r}{m}i + \frac{s}{n}k\right) \right| \quad (2.6)$$

The image matrix I_{sr} represents a truncated version of the radiating region intensity distribution function $\rho(x_r, y_s, z)$ [3]. where,

$$x_r = \left(\frac{2X}{m}\right) r, \quad y_s = \left(\frac{2Y}{n}\right) s \quad (2.7)$$

and $2X, 2Y$ are dimensions of the sample in the x and y directions respectively.

The 2DFT is implemented as two one dimensional transforms, first in the frequency encoding direction and then the phase encoding direction.

The ability to perform imaging very fast is limited by the number of increments through which the phase encoding gradient has to be stepped, as this defines image resolution. But this method is not useful for fast imaging. There have been attempts at reducing the imaging time by using short acquisition time with correction for the induced artifacts [5–7]. There have also been attempts at using Wavelet techniques for image reconstruction [8–10]. Different excitation techniques are suited for specific applications but brings additional image artifacts. But image intensity artifact is common to all the excitation techniques and should be removed for better image quality [11]. Image intensity artifact is caused by static magnetic field inhomogeneity [12, 13], bias field [14], susceptibility change [15], and relative motion between image organ and MR system [16]. The image intensity artifact makes the image useless for statistical studies, automatic segmentation and image classification [4]. Hence it is important that the intensity artifact be removed, whatever the inducing factor may be.

Our work involving the *MMF* and *PMF*, introduced in part-I of this transaction, sheds light on another mode through which image intensity artifact could be introduced in a MR image. To handle this

problem, the MR signals should be modeled accurately to include the near electromagnetic fields.

3. NEAR ELECTROMAGNETIC FIELDS IN MRI TECHNOLOGY

The signals involved in MRI are electromagnetic in nature and the coils designed to act as transceivers are in fact designed to accommodate the energy in the near electromagnetic fields [4]. Since the magnitude and phase of the near electromagnetic fields are dependent on distance, the MR temporal signals should be redefined in terms of the near electromagnetic fields.

3.1 Bloch Equations

An atomic nucleus has its own intrinsic angular momentum vector S , called spin, associated with a unique quantum number $I \equiv \{1/2(j-1); j = 1, 2, 3 \dots\}$. A nucleus with $I \neq 0$, has its own intrinsic nuclear magnetic moment m , related to S by [1]

$$m = \gamma \cdot S \quad (3.1)$$

where γ is called the gyromagnetic ratio and it depends on the type of nuclei.

In the presence of an external magnetic field $B\hat{k}$, the magnetic moment of the nucleus will experience a torque that is equal to the rate of change of the angular momentum. Hence

$$\frac{dm}{dt} = \gamma m \times B \quad (3.2)$$

But (3.2) has been obtained ignoring the interactions of the nuclei with the surrounding molecular environment (spin-lattice interaction) and those between close nuclei (spin-spin interaction). Therefore (3.2) must be modified to properly represent the macroscopic behavior of the physical system. The modifications were proposed by Bloch and is based on the following observations [3]:

- i. The changes in the spins' total energy density E are only due to spin-lattice interaction, while spin-spin interaction does not involve changes in E . Since the dominant term of $E(t)$ is $m(t) \cdot H_0(t)$, the spin-lattice interaction will contribute to the changes of $m_z(t)$.

Thus it is clear that $m_z(t)$ approaches the equilibrium value M_0 exponentially with a time constant T_1 called longitudinal or spin-lattice relaxation time, so that the rate of change of $m(t)$ due to spin-lattice interaction will be $-[m(t) - M_0]/T_1$.

- ii. Spin-spin interaction does not influence E . Hence it will not be involved in the changes of $m_z(t)$. But it will effect $m_x(t)$ and $m_y(t)$. Therefore the transversal components $m_x(t)$ and $m_y(t)$ of $m(t)$ will decrease to zero exponentially with a time constant T_2 called transversal or spin-spin relaxation time. The rates of change of $m_x(t)$ and $m_y(t)$ are $-m_x(t)/T_2$ and $-m_y(t)/T_2$ respectively.

The effect of decay of $m_x(t)$ and $m_y(t)$ due to spin-spin relaxation is stronger when the mobility of the nuclei decreases. This is the reason why the T_2 values of solids are smaller than those of liquids. Hence the transient MR signals from solids are reduced to zero much faster than those from liquids. In the MRI image solids do not appear or appear at the color code denoting the least strength. Hence the skull will appear as a dark region in a MR image whereas it will appear bright in a CT scan [2].

In order to take into account the perturbation due to spin-lattice and spin-spin interaction, the decay rates are applied to (3.2) and could be written component wise as [3]:

$$\begin{aligned}\frac{dm_x}{dt} &= \gamma [m_y H_z - m_z H_y] - \frac{m_x}{T_2} \\ \frac{dm_y}{dt} &= \gamma [m_z H_x - m_x H_z] - \frac{m_y}{T_2} \\ \frac{dm_z}{dt} &= \gamma [m_x H_y - m_y H_x] - \frac{m_z - M_0}{T_1}\end{aligned}\quad (3.3)$$

These equations are basic in MR experiments and called Bloch equations [3].

The solutions for (3.3) in the stationary plane are [3]:

$$m_x(x, t) = [m_x(x, 0) \cos \theta(x, t) - m_y(x, 0) \sin \theta(x, t)] \exp\left(-\frac{t}{T_2(x)}\right) \quad (3.4.1)$$

$$m_y(x, t) = [m_x(x, 0) \sin \theta(x, t) + m_y(x, 0) \cos \theta(x, t)] \exp\left(-\frac{t}{T_2(x)}\right) \quad (3.4.2)$$

$$m_z(x, t) = m_z(x, 0) - [m_z(x, 0) - M_0(x)] \left[1 - \exp\left(-\frac{t}{T_1(x)}\right) \right] \quad (3.4.3)$$

Equations (3.4.1) and (3.4.2) can be written as

$$m_x(x, t) = |m_{xy}(x, 0)| \exp\left(-\frac{t}{T_2(x)}\right) \cos[\theta(x, t) + \psi(x)] \quad (3.5.1)$$

$$m_y(x, t) = |m_{xy}(x, 0)| \exp\left(-\frac{t}{T_2(x)}\right) \sin[\theta(x, t) + \psi(x)] \quad (3.5.2)$$

where $m_{xy}(x, t) \equiv [m_x(x, t), m_y(x, t), 0]$ is the projection of $\underline{m}(x, t)$ on the xy plane and $\psi(x) = m_y(x, 0)/m_x(x, 0)$. From (3.5.1) and (3.5.2) it is seen that $\underline{m}(x, t)$ rotates around \underline{k} with an angular velocity of $\omega(x, t) = -\gamma H(x, t)$ (Larmor frequency) and its' projection on the xy plane decreases with a time constant T_2 . From (3.4.3) it is seen that the \underline{k} projection of $\underline{m}(x, t)$ approaches exponentially the value $M_0(x)$ with time constant T_1 .

3.2 Electromagnetic Fields due to the Resonating Nuclear Magnetic Moment

In conventional Magnetic Resonance signal analysis, the time domain signal expressions are obtained in terms of the net magnetization moment and no study has been carried out on the fields created by these magnetic moments. In analyzing the signals, the effect of the electromagnetic fields, it's interaction with the sensing coil and especially the effect of the near electromagnetic fields have not been studied.

The rotating magnetic moment in the xy -plane could be modeled by two magnetic moments that are in phase quadrature and acting along the x and y -axes. These two magnetic moments could be represented by (3.5.1) and (3.5.2) respectively. The geometrical setup of the magnetic moments is shown in Fig. 3.1.

In order to find the electric and magnetic fields due to the rotating magnetic moment, the rotating magnetic moment is replaced by two magnetic moments in the x, y directions that are in phase quadrature. This will create a rotating magnetic moment in the xy plane. The fields due to magnetic moments in the x, y directions are found separately and added in the time domain vectorially to arrive at the resultant electromagnetic fields.

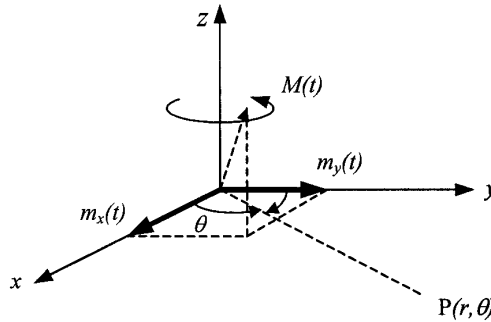


Figure 3.1 Geometrical placement of the magnetic moments.

The magnetic moment m is related to the hypothetical magnetic current I_m given by [17, 18]

$$m = I_m l \tag{3.6}$$

where l is the length of the magnetic dipole. Also the magnetic field components H_r and H_θ of a magnetic dipole of length l could be written as [17]

$$H_r = \frac{I_m l \cos \theta}{2\pi\eta r^2} \left[1 + \frac{1}{jkr} \right] e^{-jkr} \tag{3.7}$$

$$H_\theta = j \frac{k I_m l \sin \theta}{4\pi\eta r} \left[1 + \frac{1}{jkr} - \frac{1}{(kr)^2} \right] e^{-jkr} \tag{3.8}$$

3.2.1 Magnetic Fields due to the Magnetic Moment Along the x axis

Substituting for magnetic moment $I_m l$ using (3.5.1), the magnetic field components due to $m_x(t)$ is found to be

$$H_{rX}(t) = \frac{m_{xy} e^{-t/T_2} \cos \theta}{2\pi\eta} \frac{\cos \theta}{r^2} \left[1 + \frac{1}{jkr} \right] \cos [\omega_0 t + \psi(x) - kr] \tag{3.9}$$

$$H_{\theta X}(t) = \frac{k m_{xy} e^{-t/T_2} \sin \theta}{4\pi\eta} \frac{\sin \theta}{r} \left[1 + \frac{1}{jkr} - \frac{1}{(kr)^2} \right] \sin [\omega_0 t + \psi(x) - kr] \tag{3.10}$$

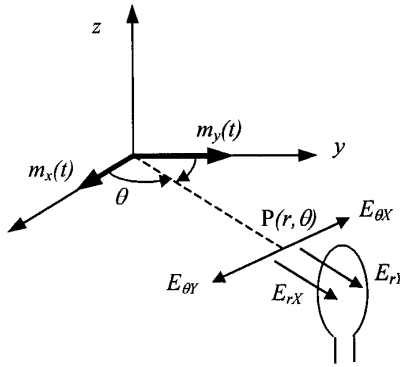


Figure 3.2 Magnetic field components due to the two magnetic moments.

3.2.2 Magnetic Fields due to the Magnetic Moments Along the y axis

Substituting for magnetic moment $I_m l$ using (3.5.2), the magnetic field components due to $m_y(t)$ are found to be:

$$H_{rY} = \frac{m_{xy}e^{-t/T_2}}{2\pi\eta} \frac{\cos(90^\circ - \theta)}{r^2} \left[1 + \frac{1}{jkr} \right] \sin [\omega_0 t + \psi(x) - kr]$$

which reduces to

$$H_{rY} = \frac{m_{xy}e^{-t/T_2}}{2\pi\eta} \frac{\sin \theta}{r^2} \left[1 + \frac{1}{jkr} \right] \sin [\omega_0 t + \psi(x) - kr] \quad (3.11)$$

The θ component of the magnetic field is given by

$$H_{\theta Y}(t) = -j \frac{km_{xy}e^{-t/T_2}}{4\pi\eta} \frac{\sin(90^\circ - \theta)}{r} \left[1 + \frac{1}{jkr} - \frac{1}{(kr)^2} \right] \sin [\omega_0 t + \psi(x) - kr]$$

which reduces to

$$H_{\theta Y}(t) = -\frac{km_{xy}e^{-t/T_2}}{4\pi\eta} \frac{\cos \theta}{r} \left[1 + \frac{1}{jkr} - \frac{1}{(kr)^2} \right] \sin [\omega_0 t + \psi(x) - kr] \quad (3.12)$$

3.2.3 Resultant Magnetic Fields at $P(r, \theta)$

The resultant magnetic field components at an observation point $P(r, \theta)$ are found by the vector sum of the individual components, and may be expressed as

$$H_R(t) = H_{rX}(t) + H_{rY}(t) \quad (3.13)$$

$$H_\theta(t) = H_{\theta X}(t) - H_{\theta Y}(t) \quad (3.14)$$

Substituting (3.9) and (3.11) into (3.13), we get

$$H_R = \frac{m}{2\pi\eta} \frac{e^{-t/T_2}}{r^2} \left[1 + \frac{1}{jkr} \right] \{ \cos \theta \cos [\omega_0 t + \psi(x) - kr] \\ + \sin \theta \sin [\omega_0 t + \psi(x) - kr] \}$$

which reduces to

$$\boxed{H_R = \frac{m}{2\pi\eta} \frac{e^{-t/T_2}}{r^2} \left[1 + \frac{1}{jkr} \right] \cos [\omega_0 t + \psi(x) - kr - \theta]} \quad (3.15)$$

Substituting (3.10) and (3.12) into (3.14), we get

$$H_\theta(t) = \frac{km}{4\pi\eta} \frac{e^{-t/T_2}}{r} \left[1 + \frac{1}{jkr} - \frac{1}{(kr)^2} \right] \{ \cos \theta \cos [\omega_0 t + \psi(x) - kr] \\ - \sin \theta \sin [\omega_0 t + \psi(x) - kr] \}$$

which reduces to

$$\boxed{H_\theta(t) = \frac{km}{4\pi\eta} \frac{e^{-t/T_2}}{r} \left[1 + \frac{1}{jkr} - \frac{1}{(kr)^2} \right] \cos [\omega_0 t + \psi(x) - kr + \theta]} \quad (3.16)$$

Equations (3.15) and (3.16) gives the resultant magnetic field components in the radial and tangential directions on the xy plane respectively.

3.3 Magnetic Resonance Time Domain Signal

There exists a changing magnetic field near a sample excited by an external magnetic field \underline{H} as seen from (3.15) and (3.16). Thus, a

coil placed near the sample with its axis on the xy plane will detect a voltage induced in it by electromagnetic induction. This is the only measurable quantity in a MR experiment and image reconstruction is done using these measurements.

To find the voltage induced in a coil, it is necessary to find the flux linkage in the coil due to the magnetic field. The flux linkage ϕ_n is defined as

$$\phi_n = \underline{B} \cdot \underline{A} = \mu \underline{H} \cdot \underline{A} \quad (3.17)$$

where \underline{A} is the area of the coil and uniform flux distribution over the coil area is assumed. When the coil is placed in a position to pick up only the radial component of the magnetic field, (3.17) becomes

$$\phi_n = \mu H_R A$$

assuming that the magnetic field H_R is uniform within the area A of the coil. The induced voltage or current in the coil is the time derivative of the flux linkage through the coil [18]. Hence the current is given by

$$\begin{aligned} i(t) &= -C \frac{d\phi_n}{dt} \quad \text{for } t \geq t_d \\ i(t) &= -C \frac{\mu m A}{2\pi\eta} \frac{1}{r^2} \left[1 + \frac{1}{jkr} \right] \frac{d}{dt} \left\{ e^{-t/T_2} \cos [\omega_0 t + \psi(x) - kr - \theta] \right\} \\ &= -C \frac{\mu m A}{2\pi\eta} F_R(r) \frac{d}{dt} \left\{ e^{-t/T_2} \cos [\omega_0 t + \psi(x) - kr - \theta + \alpha(r)] \right\} \end{aligned}$$

where

$$F_R(r) = \sqrt{\frac{1}{r^4} + \frac{1}{k^2 r^6}} \quad (3.18)$$

$$\alpha(r) = \tan^{-1} \left(-\frac{1}{kr} \right) \quad (3.19)$$

$$\begin{aligned} i(t) &= -C \frac{\mu m A}{2\pi\eta} e^{-t/T_2} F_R(r) \left\{ -\omega_0 \sin [\omega_0 t + \psi(x) - kr - \theta + \alpha(r)] \right. \\ &\quad \left. - \frac{1}{T_2} \cos [\omega_0 t + \psi(x) - kr - \theta + \alpha(r)] \right\} \quad (3.20) \end{aligned}$$

Note that $\eta = \sqrt{\frac{\mu}{\epsilon}}$, $\nu = \frac{1}{\sqrt{\mu\epsilon}}$ and wave-number $k = \frac{\omega_0}{\nu}$. Substituting for these parameters, (3.20) becomes

$$i(t) = -C \frac{mAF_R(r)}{2\pi} e^{-t/T_2} \left\{ \begin{array}{l} -k \sin [\omega_0 t + \psi(x) - kr - \theta + \alpha(r)] \\ -\frac{1}{\nu T_2} \cos [\omega_0 t + \psi(x) - kr - \theta + \alpha(r)] \end{array} \right\} \quad (3.21)$$

Here ν is in the order of 10^8 and T_2 in the order of 10^{-3} [1]. In comparison to the first term of (3.21), the second term will be negligibly small. Thus (3.21) simplifies to,

$$i(t) \approx C \frac{km}{2\pi} F_R(r) e^{-t/T_2} \sin [\omega_0 t + \psi(x) - kr - \theta + \alpha(r)] \quad (3.22)$$

Considering the time delay t_d in the signal reaching the receiver, (3.22) could be re-written as,

$$i(t) = C \frac{km}{2\pi} F_R(r) e^{-\overline{t-t_d}/T_2} \cdot \sin [\omega_0(t - t_d) + \psi(x) - \theta + \alpha(r)] u(t - t_d) \quad (3.23)$$

where the time delay t_d is defined as $t_d = \frac{r}{\nu}$ and $u(t)$ denotes the step function.

3.3.1 Ensemble of Signals from Radiating Regions

A sample under test will have numerous radiating regions. But to show peculiar effects due to the individual radiating regions, the ensemble of signals obtained is modeled as a discrete summation. The signals thus obtained may be expressed as

$$x(t) = C \frac{km}{2\pi} \sum_i F_R(r_i) e^{-\overline{t-t_{di}}/T_2} \sin [2\pi f_0(t - t_{di}) + \psi(x) - \theta(i) + \alpha(r_i)] u(t - t_{di}) \quad (3.24)$$

where $F_R(r_i)$ is the *MMF*, which depends on the distance between the radiating region i and the receiver; t_{di} is the time delay in the signal reaching the receiver; $\psi(x)$ is a constant phase; $\theta(i)$ is a phase angle depending on the placement of the receiver coil; $\alpha(r_i)$ is a distance dependent phase term due to the complex nature of the near fields and

$u(t)$ is a step function. The integer i will vary over the number of radiating regions.

In MR experiments, signals are obtained using frequency and phase encoding field gradients, in which case the signal described in (3.24) should be modified to include different frequencies and phase. Thus (3.24) becomes

$$x(t) = C \frac{km}{2\pi} \sum_i \sum_j F_R(r_i) e^{-\overline{t-t_{di}}/T_2} \sin [2\pi f_i(t - t_{di}) + \psi(x) - \theta(i) + \alpha(r_i) + \phi_j] u(t - t_{di}) \tag{3.25}$$

where ϕ_j is the phase angle due to the phase encoding gradient. Thus, the signal of (3.25) is encoded in frequency and phase. The frequency f_i and phase ϕ_j are defined as

$$f_i = f_0 + g_f i = f_0 + \Delta f \tag{3.26}$$

$$\phi_j = g_p j \tag{3.27}$$

where g_f, g_p are the frequency and phase encoding gradients respectively and i, j are aliases for distance used here in a discrete sense and span over the number of frequency and phase encoding steps.

For illustrative purposes, nine discrete radiating regions are selected on a square, as shown in Fig. 3.3. This set up has been selected to study the effects of the frequency and phase encoding gradients on the near-field MRI signals and also to show the effect due to the *MMF* in modulating the signal strength from region to region.

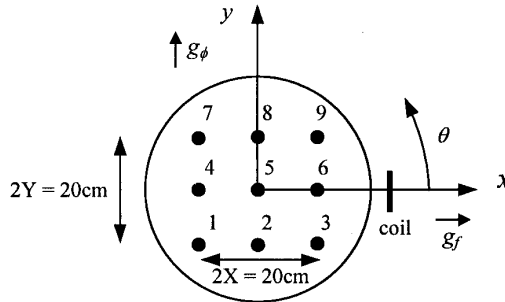


Figure 3.3 Radiating regions under study.

The receiving coil is placed perpendicular to the x -axis. This set up simplifies the calculations.

The radiating regions are assumed to be resonating at 100 MHz, corresponding to $\gamma = 50 \times 10^6$ at a field strength of 2 Tesla. These signals are stepped down in frequency by coherent quadrature demodulation which enables the phase information to be retrieved. For this purpose, the local oscillator frequency was assumed to be 99.5 MHz. Thus, the center frequency is 0.5 MHz (500 kHz). The relaxation time constant T_2 was assumed to be 0.003 s, a realistic value closely matching a practical situation [1]. The other phase angle $\alpha(r)$ is calculated from (3.19). The magnetization density m is assumed to be $4.4 \times 10^{-3} \text{ Am}^{-2}$. When a field gradient (g_f) of 1mT/cm is applied, the corresponding change in frequency can be calculated from

$$\Delta f = \frac{\gamma \cdot g_f}{2\pi} \quad (3.28)$$

Substituting the values of γ and g_f , we get $\Delta f \approx 8750 \text{ Hz/cm}$. Similarly, phase gradient of $3.75^\circ/\text{cm}$ is assumed. Thus for the radiating regions considered, the frequency difference between regions (1, 4, 7), (2, 5, 8) and (3, 6, 9) in Fig. 3.3 will be

$$\begin{aligned} \Delta f &= 8750 \times 10 \\ &= 87.5 \text{ kHz} \end{aligned}$$

The relative phase difference between regions (1, 2, 3), (4, 5, 6) and (7, 8, 9) will be

$$\begin{aligned} \Delta\phi &= 3.75 \times 10 \\ &= 37.5^\circ \end{aligned}$$

The signals from the different regions are shown in Fig. 3.4.

In Fig. 3.4, the signals in each column have identical frequency and it is progressively increasing from left to right column. This is due to a positive frequency-encoding field gradient in the x -direction. The starting phases of the signals in a row are approximately identical. This is because the phase-encoding field gradient is applied in the y -direction and it does not affect the signal phase in the x -direction. The small perturbations are due to the additional phase quantities defined in (3.25). This includes the distant dependent *PMF* too. It is seen that the amplitude of the signal from region-6 determines the magnitude of the resultant signal.

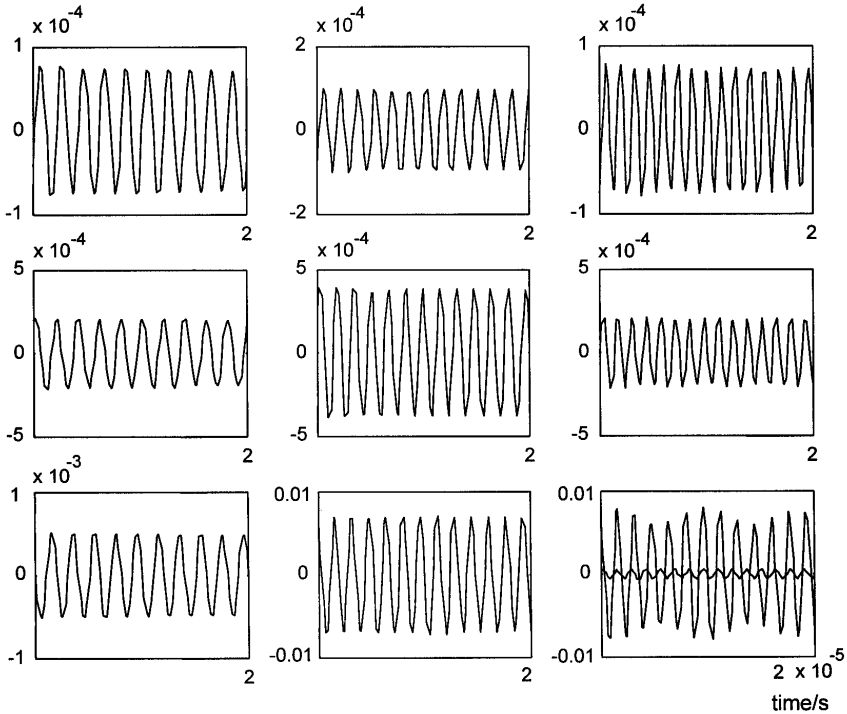


Figure 3.4 Magnetic resonance signals.

The nine regions were assigned equal radiating strengths i.e. equal magnetization density. Hence the initial amplitude of the received signal has to be equal. But as seen from Fig. 3.4, it is not. This is due to the effect of the MMF , $F_R(r)$. Depending on the distance between the coil and the radiating regions, the amplitude of the signal is changed. The variation of the MMF and PMF with distance is shown in Fig. 3.5 and Fig. 3.6, respectively.

As demonstrated in Fig. 3.5, the factor $F_R(r)$ varies rapidly and is large when the distance r is small. Hence the amplitude of the signal from region-6, which is the closest to the coil, is the largest. The difference in the signal amplitude from different regions could be as large as 14 dB. From Fig. 3.6 it is seen that the variation of the PMF due to H_r does not change rapidly with distance. Hence for the nine radiating regions of Fig. 3.3, there will be negligible variation in phase introduced due to the PMF . In the more complete signal model proposed in (3.25), it is possible to account for the additional phase and amplitude perturbations due to the near-field phenomena.

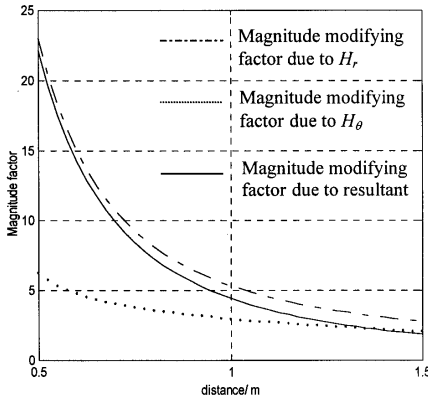


Figure 3.5 Variation of magnitude modifying factor.

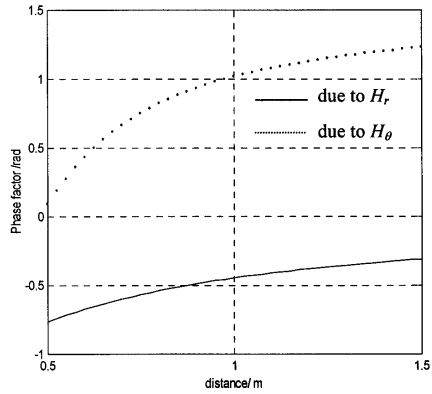


Figure 3.6 Variation of the phase modifying factor.

4. MAGNETIC RESONANCE IMAGE RESULTS

In order to see the effects of the additional phase and amplitude modulation factors on image synthesis, the nine radiating regions shown in Fig. 3.3 are imaged using Fourier imaging techniques. We ignore the effects of the complex impedance of the different materials present in the human body and the interaction of these materials with the resonating magnetic dipoles. The complex impedance of the bio-materials and the net effect due to the interactions can be considered as a random phase noise and compensated for [19]. The simplified signal model that ignores this random phase noise is used to illustrate the effects due to the near EM fields in MRI.

4.1 H_r based Image

The image of the nine radiating regions when the signal is modified by the *MMF* of the radial magnetic field component is shown in Fig. 4.1. Although the intensities of the nine regions should be equal as per the assigned magnetization density values, they are not identical in the image.

The relative image intensity of regions 1 to 9 from Fig. 4.1 is 1 : 1.71 : 4 : 1.14 : 2 : 5.43 : 1 : 1.71 : 4. The relative error in image intensity is as large as 9 dB between the extreme values. This will render the image unreliable for statistical studies, segmentation and classification.

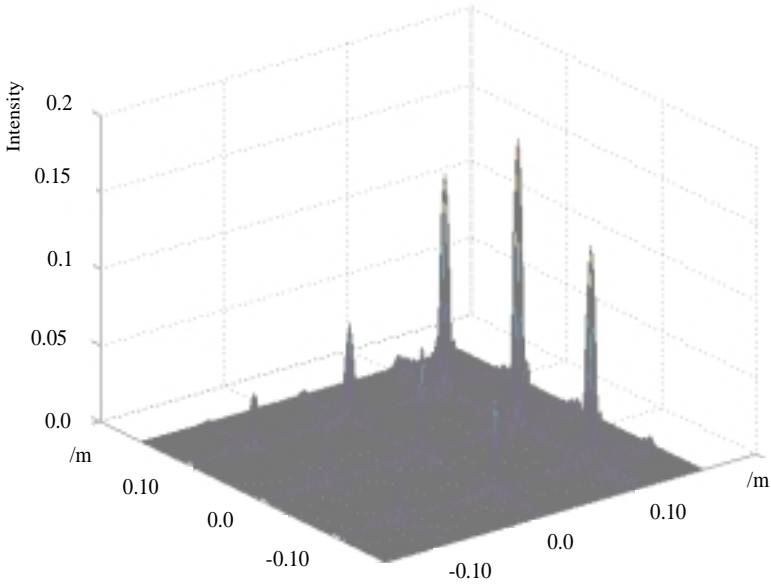


Figure 4.1 Perspective view of H_r based image.

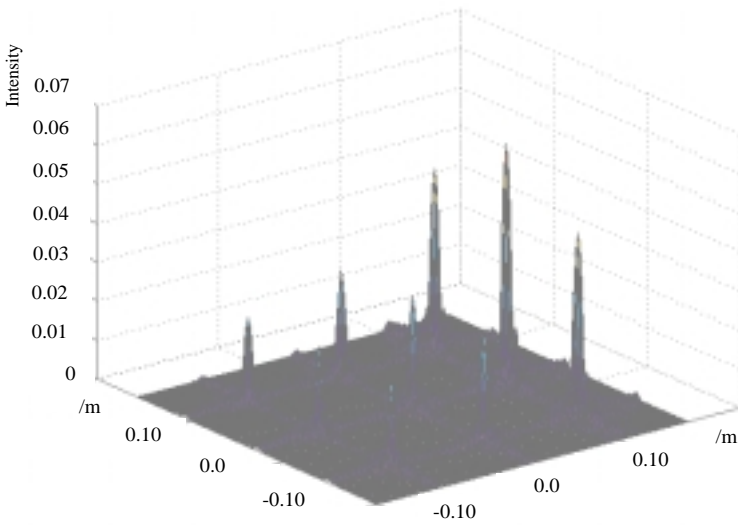


Figure 4.2 Perspective view of H_θ based image.

4.2 H_θ based Image

Fig. 4.2 shows the H_θ based image of the nine regions described in Fig. 6.3. The relative image intensities of regions 1 to 9 are 1 : 1.3 : 2.24 : 1.05 : 1.38 : 2.95 : 1 : 1.3 : 2.24 respectively. The maximum image intensity error is small when compared with that for the H_r based image. The maximum relative error was calculated to be less than 5 dB. Hence it is seen that the images obtained with H_θ based signals are better than that obtained with H_r signals.

4.3 Image due to Circularly Polarized Signals

In the near field region of the electromagnetic signals, two orthogonal magnetic fields H_r and H_θ are present. In MRI technology the receiving coils are usually placed in the near field region. Hence the resultant received signals are circularly polarized. If the receiver is capable of picking up the circularly polarized signal, which is the current MRI practice, the MR signal magnitude will be modified by the resultant MMF defined by

$$F(r) = \sqrt{F_r^2 + F_\theta^2} \quad (4.1)$$

The image obtained for the nine-region test case with such a circularly polarized signal is shown in Fig. 4.3. The relative image intensity ratio for regions 1 to 9 is 1 : 1.7 : 3.75 : 1.10 : 1.95 : 5 : 1 : 1.7 : 3.75. The maximum deviation in intensity is 7.2 dB. It is apparent that the reconstructed image resembles the image from H_r .

In all the three cases considered using H_r, H_θ or $\sqrt{H_r^2 + H_\theta^2}$ the images do not represent the information accurately. Based on the simulation and theoretical studies carried out, it is established that the images obtained through imaging routines currently in use do not convey the information accurately. The image misrepresentation due to near-field effects can be classified as image intensity inhomogeneity. This error has been unaccounted for because the incompleteness of the underlying signal model used in current MRI machines and its implications to the imaging routine have not been studied. Although image intensity inhomogeneity due to the external magnetic field inhomogeneity has been analyzed and correction measures proposed in [20, 21] the near field effects have been ignored.

Since a more complete signal model has been proposed in this paper, it is possible to account for this additional error in intensity and

perform a correction for the image intensity inhomogeneity. This procedure is explained in the next section.

5. CORRECTION FOR INTENSITY INHOMOGENEITY ARTIFACT

5.1 Correction for Phase Modifying Factor

Erroneous phase information will distort the image geometry and intensity. The radiating regions in an image will be misregistered in position, modulated in intensity and scaled in size. It has been noted that the phase information is corrupted due to inhomogeneity in the B_1 field and due to the susceptibility change near bone-tissue and tissue-air interfaces. A variety of correction procedures have been proposed. In [15], a set of reference scans has been obtained with homogenous material as subject and the correct phase information thus derived has been utilized to correct the distorted phase information in the actual routine. Images obtained through this procedure are seen to be satisfactory. But the distant dependent phase information has not been removed by this procedure and will distort the image. Phase can be corrupted through coil imperfection and alterations to its nominal position with respect to the patient [14]. This image distortion has been termed as *coil effect* and attributed to a bias field. Although this effect can be ignored for qualitative analysis, it is important for automated image segmentation activity. The bias field has been estimated and corrected using phantom images [11] and polynomial fitting [12]. But these methods are based on assuming that the corrupting effects are patient independent, which is not correct. It has been found that the correction should be done retrospectively and also that *post*-filtering is better than *pre*-filtering [14]. Our approach in correcting for the phase and magnitude modifying factors are post processing steps and thus highly suitable for this problem. In addition, image artifacts are created through phase distortion due to static field inhomogeneity [13], relative motion of patient [16] and $N/2$ ghost artifact due to non-optimum data acquisition system performance [22].

The variation of *PMF* due to H_r and H_θ with distance, as shown in Fig. 3.6, is not rapid. As such, the phase variation between signals from adjacent regions is not marked. Thus there is imperceptible intensity and mis-positioning differences in the images obtained. The image domain data in this thesis have not been corrected for phase

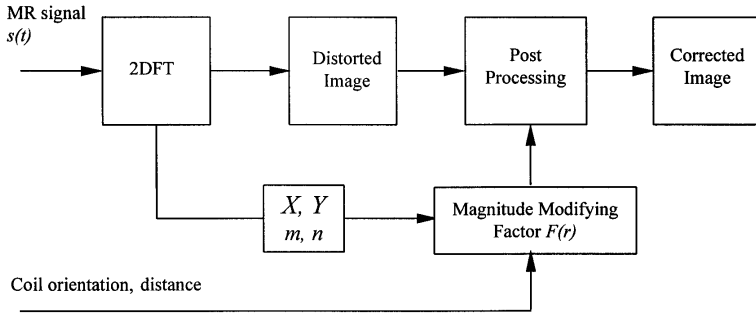


Figure 5.1 Schematic diagram of correction process.

perturbations but corrected for the more notable changes in intensity due to the *MMF*. If phase correction is to be incorporated, the correction for *PMF* should be performed before the correction for *MMF*, as detailed in [15].

5.2 Correction Algorithm for Magnitude Modifying Factor

The knowledge of the underlying near field MR signal enables a correction procedure to be incorporated in the imaging routine. This procedure is to operate on the distorted image and the algorithm is shown schematically in Fig. 5.1. The procedure could be explained as follows:

- The image is formed using Fourier imaging technique, as shown in the upper first two blocks in Fig. 5.1.
- The imaging routine determines the resolution and the field of view. Hence the parameters m, n and X, Y are known, where m, n are the number of points processed in the x, y directions respectively; X, Y are the object dimension in the x, y directions respectively with reference to Fig. 3.3. These data are fed to the MMF black box.
- The orientation and distance of the coil with respect to the fixed axis system, as shown in Fig. 3.3 are also fed to the MMF black box. The orientation could be detected by the signal pickup electronic system. The distance is usually a fixed parameter. Depending on coil orientation, an appropriate signal model is chosen.
- The MMF is computed and fed to the post processor, which incorporates this factor to correct the distorted image. The end result is the corrected image.

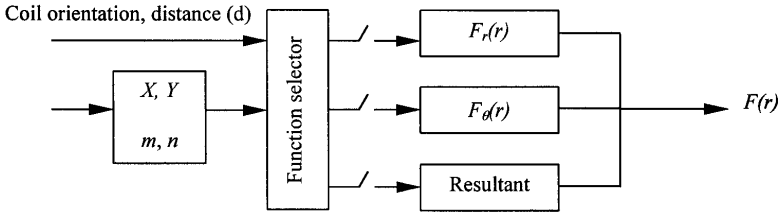


Figure 5.2 MMF block.

The MMF and post processor blocks are discussed in sections 5.2.1 and 5.2.2 respectively.

5.2.1 MMF Block

The input parameters and the function of the MMF block could be further detailed as shown in Fig. 5.2. Depending on the orientation of the pickup coil, the receiver picks up the H_r, H_θ or the circularly polarized resultant signal. When the coil receives the H_r component, there will be contribution from the H_θ component as well. Hence the usual signal to be used in processing is that due to the resultant and it is evident from image results and analysis of the MMF that the resultant factor follows the response of H_r . Hence the coil orientation should be selected correctly for optimum performance.

The field of view parameter gives the values of X and Y . Further, the number of points used for the 2DFT operation (m, n) are known since it is set by the operator. The calculation is done using (2.7), and repeated here for convenience:

$$x_p = \left(\frac{2X}{m}\right) p \quad y_p = \left(\frac{2Y}{n}\right) q$$

where p, q are the parameters of the image domain data $I(p, q)$. The distance to the radiating region from the receiver is calculated from

$$r_{pq} = \sqrt{(d - x_p)^2 + y_q^2} \tag{5.1}$$

where d is the distance of the coil-center from the origin of the axis system. Once the distance is known the corresponding factor could be calculated for each point on the image. Thus the output of the MMF block is a spatial filter $S(p, q)$.

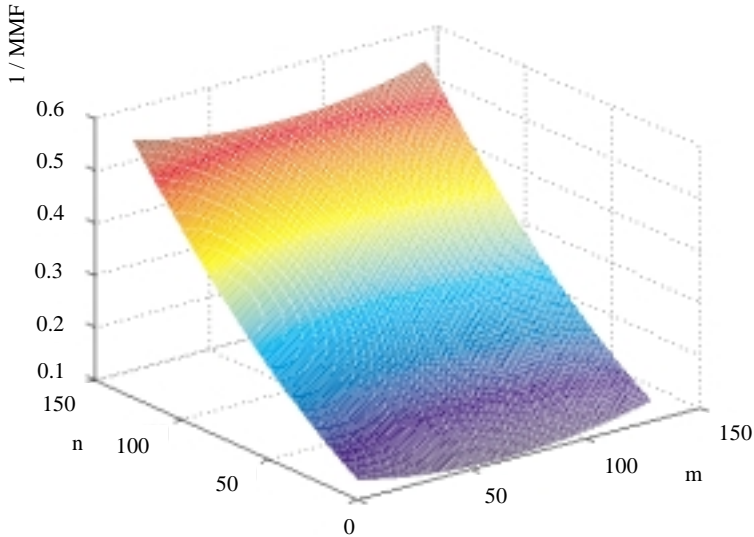


Figure 5.3 Spatial filter of order 128×128 for field of view of 20×20 cm.

To reduce the computational effort, the image could be segmented and the filter coefficients computed for only a fraction of the total number of image pixels. This is feasible since there will not be abrupt intensity changes within a few pixels in the image. Also the circular symmetry of the problem (if applicable) could be used to halve the number of points required for distance calculation. Hence for a 128×128 order filter, calculations on 64×64 points are sufficient. The filter coefficients could be saved on computer disk and need not be computed every time.

The spatial filter is given by

$$S(p, q) = 1/F(r_{pq}) \quad (5.2)$$

Such a filter response is shown in Fig. 5.3. Here the field of view and the number of points for resolution calculation were taken to be 20×20 cm and 128×128 respectively.

Equal coefficients are shown with the same color on the graph. The color changes gradually signifying the fact that the coefficients do not change rapidly. Also the filter coefficients are symmetrical about the x -axis. Due to this property of symmetry, the computational requirement could be reduced by half as mentioned earlier.

5.2.2 Post Processing Block

The corrected image domain data $I'(p, q)$ could be obtained by the following operation:

$$I'(p, q) = I(p, q) \cdot S(p, q); \quad p, q : -\frac{1}{2}N, -\frac{1}{2}N + 1, \dots, \frac{1}{2}N - 1 \quad (5.3)$$

where the order of the spatial filter is identical to that of the image domain dimension N . When a reduction factor R is used on the order of the filter, the operation could be defined by

$$I'(p, q) = I\left(\frac{p}{R}, \frac{q}{R}\right) \cdot S(a, b); \quad \text{ceiling}(p/R, q/R) : 1, 2, \dots, N/R \\ a, b : 1, 2, \dots, N/R \quad (5.4)$$

where *ceiling* gives the nearest upper integer value. The resolution afforded by the corrected image depends on the order of the spatial filter.

5.3 Corrected Image

The distorted image of Fig. 4.3 was filtered by the MMF filter and the resultant image is shown in Fig. 5.4. The nine radiating regions shown in Fig. 5.4 have equal radiating strengths after the filtering process. This image is more useful for clinical diagnosis and statistical studies since the image of Fig. 5.4 does not have the intensity inhomogeneity artifact.

6. CONCLUSIONS

It has been demonstrated that the resonating atomic nuclei in the human body can be modeled by a collection of infinitesimal magnetic dipoles. This allows for the proper modeling of the magnetic resonance signals by incorporating the hitherto unaccounted near electromagnetic fields. Two new factors, namely *Magnitude Modifying Factor* and *Phase Modifying Factor*, have been introduced. It is shown that the current MR images contain residual intensity artifact due to the *MMF* and *PMF*. Using the more accurate signal model proposed, a revised imaging algorithm is presented that alleviates the inherent intensity artifact found in MR images.

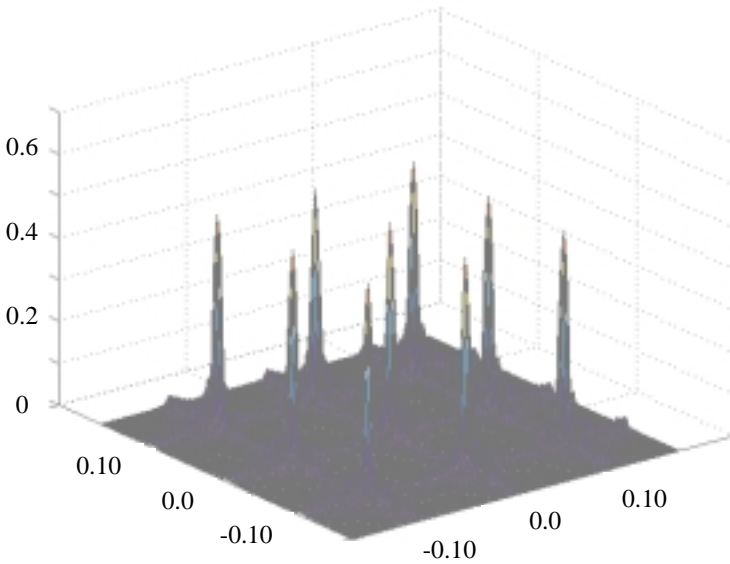


Figure 5.4 Corrected MR image of nine radiating regions.

REFERENCES

1. Chen, C. N., and D. I. Hoult, *Biomedical Magnetic Resonance Technology*, AdamHilger, Bristol, New York, 1989.
2. Jin, J. M., *Electromagnetic Analysis and Design in Magnetic Resonance Imaging*, CRC Press, Boca, Raton, FL, 1998.
3. Sebastiani, G., and P. Barone, "Mathematical principles of basic magnetic resonance imaging in medicine," *Signal Processing*, 1991.
4. Hornak, P., "Magnetic resonance imaging-a hypertext," www.rit.edu/htbooks.
5. Barone, P., and G. Sebastiani, "A new method of magnetic resonance image reconstruction with short acquisition time and truncation artifact reduction," *IEEE trans. Med. Imaging*, Vol. 11, No. 2, June 1992.
6. Oh, S., C. Ramon, R. J. Marks, A. C. Nelson, and M. G. Meyer, "Resolution enhancement of biomagnetic images using the method of alternating projections," *IEEE trans. Biomed. Eng.*, Vol. 40, No. 4, April 1993.
7. Oskoui, P., and H. Stark, "A comparative study of three reconstruction methods for a limited-view computer tomography problem," *IEEE trans. Med. Imaging*, Vol. 8, No. 1, March 1989.

8. Panych, L. P., "Theoretical comparison of Fourier and Wavelet encoding in magnetic resonance imaging," *IEEE trans. Med. Imaging*, Vol. 15, No. 2, April 1996.
9. Sahiner, B., and A. E. Yagle, "Image reconstruction from projections under Wavelet constraints," *IEEE Trans. Signal Processing*, Vol. 41, No. 12, December 1993.
10. Bhatia, M., and W. C. Karl, "A Wavelet-based method for multiscale tomographic reconstruction," *IEEE Trans. Med. Imaging*, Vol. 15, No. 1, February 1996.
11. Wicks, D. A., G. J. Barker, and P. S. Tofts, "Correction of intensity nonuniformity in MR images for sensitivity of the surface coil," *Magn. Reson. Imag.*, Vol. 11, 183–196, 1993.
12. Tincher, M., C. R. Meyer, R. Gupta, and D. M. Williams, "Polynomial modelling and reduction of spatial body-coil spatial inhomogeneity," *IEEE Trans. Med. Imaging*, Vol. 12, 361–365, 1993.
13. Reichenbach, J. R., R. Venkatesan, D. A. Yablonskiy, M. R. Thompson, S. Lai, and E. M. Haacke, "Theory and application of static field inhomogeneity effects in gradient-echo imaging," *J. Magn. Reson.*, Vol. 7, 266–279, 1997.
14. Guillemaud, R., and M. Brady, "Estimating the bias field of MR Images," *IEEE trans. Med. Imaging*, Vol. 16, No. 3, June 1997.
15. Wan, X., G. T. Gullberg, D. L. Parker, and G. L. Zeng, "Reduction of geometric and intensity distortions in echo-planar imaging using a multireference scan," *Magn. Reson. Med.*, Vol. 37, 932–944, 1997.
16. Wu, D. H., J. S. Lewin, and J. L. Duerk, "Inadequacy of motion correction algorithms in functional MRI: role of susceptibility-induced artifacts," *J. Magn. Reson.*, Vol. 7, 365–370, 1997.
17. Balanis, C. A., *Antenna theory: Analysis and Design*, Harper and Row, New York, 1982.
18. Hoole, S. R. H., and P. R. P. Hoole, *Engineering Electromagnetics*, Oxford University Press, Oxford, 1996.
19. Naveendra, T. S., and P. Hoole, "Complex impedance materials in medical imaging," *Proc. IMRE*, Singapore, March 1998.
20. Chang, H., and J. M. Fitzpatrick, "A technique for accurate magnetic resonance imaging in the presence of field inhomogeneities," *IEEE Trans. Med. Imaging*, Vol. 11, No. 3, September 1992.
21. Meyer, C. R., P. H. Bland, and J. Pipe, "Retrospective correction of intensity inhomogeneities in MRI," *IEEE Trans. Med. Imaging*, Vol. 14, No. 1, March 1995.
22. Buonocore, M. H., and L. Gao, "Ghost artifact reduction for echo planar imaging using image phase correction," *Magn. Reson. Med.*, Vol. 38, 89–100, 1997.